

Hydrothermal Synthesis

SPECIAL
ISSUESolution-Based, Anion-Doping of $\text{Li}_4\text{Ti}_5\text{O}_{12}$ Nanoflowers for Lithium-Ion Battery ApplicationsKenna L. Salvatore^{+, [a]}, Diana M. Lutz^{+, [a]}, Haoyue Guo,^[a] Shiyu Yue,^[a] Joceline Gan,^[a]
Xiao Tong,^[b] Ping Liu,^[c] Esther S. Takeuchi,^[a, d, e] Kenneth J. Takeuchi,^[a, d]
Amy C. Marschilok,^{*[a, d, e]} and Stanislaus S. Wong^{*[a]}

Abstract: Solution-based, anionic doping represents a convenient strategy with which to improve upon the conductivity of candidate anode materials such as $\text{Li}_4\text{Ti}_5\text{O}_{12}$ (LTO). As such, novel synthetic hydrothermally-inspired protocols have primarily been devised herein, aimed at the large-scale production of unique halogen-doped, micron-scale, three-dimensional, hierarchical LTO flower-like motifs. Although fluorine (F) doping has been explored, the use of chlorine (Cl) dopants is the primary focus here. Several experimental variables, such as dopant amount, lithium hydroxide concentration, and titanium butoxide purity, were probed and perfected. Furthermore, the Cl doping process did not damage the intrinsic LTO morphology. The analysis, based on interpreting a compilation of SEM, XRD, XPS, and TEM-EDS results, was

used to determine an optimized dopant concentration of Cl. Electrochemical tests demonstrated an increased capacity via cycling of 12% for a Cl-doped sample as compared with pristine LTO. Moreover, the Cl-doped LTO sample described in this study exhibited the highest discharge capacity yet reported at an observed rate of 2C for this material at 143mAhg^{-1} . Overall, these data suggest that the Cl dopant likely enhances not only the ion transport capabilities, but also the overall electrical conductivity of our as-prepared structures. To help explain these favorable findings, theoretical DFT calculations were used to postulate that the electronic conductivity and Li diffusion were likely improved by the presence of increased Ti^{3+} ion concentration coupled with widening of the Li migration channel.

[a] K. L. Salvatore,⁺ D. M. Lutz,⁺ Dr. H. Guo, Dr. S. Yue, J. Gan, Dr. E. S. Takeuchi, Dr. K. J. Takeuchi, Dr. A. C. Marschilok, Dr. S. S. Wong
Department of Chemistry
State University of New York at Stony Brook
Stony Brook, NY 11794-3400 (USA)
E-mail: amy.marschilok@stonybrook.edu
stanislaus.wong@stonybrook.edu

[b] Dr. X. Tong
Center for Functional Nanomaterials, Building 735
Brookhaven National Laboratory
Upton, NY 11973 (USA)

[c] Dr. P. Liu
Chemistry Department, Building 555
Brookhaven National Laboratory
Upton, NY 11973 (USA)

[d] Dr. E. S. Takeuchi, Dr. K. J. Takeuchi, Dr. A. C. Marschilok
Department of Materials Science and Chemical Engineering
State University of New York at Stony Brook
Stony Brook, NY 11794-2275 (USA)

[e] Dr. E. S. Takeuchi, Dr. A. C. Marschilok
Energy and Photon Sciences Directorate
Interdisciplinary Sciences Building, Building 734
Brookhaven National Laboratory
Upton, NY 11973 (USA)

[⁺] These authors contributed equally to this manuscript.

Supporting information and the ORCID identification number(s) for the author(s) of this article can be found under:
<https://doi.org/10.1002/chem.202002489>.

Part of a Special Issue on Low Temperature Solution Route Approaches to Oxide Functional Nanoscale Materials.

Introduction

The spinel $\text{Li}_4\text{Ti}_5\text{O}_{12}$ (LTO) material for Li-ion batteries, stands apart from other candidates due to its outstanding features. These include 1) a „zero-volume“ change during the Li^+ insertion and de-insertion process, which can lead to stability and cycling performance metrics that are clearly superior to graphite;^[1] 2) a high and stable charge/discharge voltage plateau around 1.55 V versus Li^+/Li , which lies above the reduction potential of electrolyte solvents, thereby not only preventing the formation of a solid electrolyte interphase (SEI) layer but also reducing the degree of Li dendrite formation; 3) its unique cubic spinel structure (i.e., space group symmetry $Fd\bar{3}m$), incorporating empty sites for enabling lithium ion mobility;^[2] and 4) its high thermal stability and overall ease of fabrication. However, as an insulating material, its low intrinsic electronic conductivity (i.e., 10^{-13} – 10^{-9} S cm)^[3] and relatively sluggish Li-ion diffusion coefficients (estimated to be 10^{-8} – 10^{-13} cm^2s^{-1})^[4] limit its overall applicability.

The use of ion doping therefore represents a practical way to improve upon the electron conductivity of LTO materials in two key aspects. First, as an intrinsic insulator, the calculated band gap of LTO is about 2 eV, which corresponds to the gap between the occupied O p-state and the empty Ti d-states.^[5] Doping in ions with various charges can potentially drive the partial transformation of Ti^{4+} into Ti^{3+} . Based upon charge compensation considerations, this move would increase the

concentration of electrons within the 3d orbitals and thereby result in enhanced conductivity. Second, dopant ions with larger sizes could induce a favorable lattice expansion, which could thereby not only enlarge the size but also increase the number of possible lithium ion diffusion pathways, with a similar net enhancement effect upon the ionic conductivity of LTO.^[6] A number of prior, relevant studies of doped LTO materials exist.

For cubic LTO, Cr³⁺ and Mg²⁺ dopants mainly occupy the 16*d* sites, whereas Fe³⁺ and Ni³⁺ dopants are predominantly localized at the 8*a* sites, which have been shown to hinder Li⁺ ion transport, according to previous DFT calculations.^[7] Within a triclinic structure of LTO, Zn²⁺ ions prefer the Li 8*a* sites,^[8] whereas Gd³⁺^[9] and Ca²⁺ ion dopants^[10] favor the Li 16*d* site. Anions, such as F⁻, Cl⁻ and Br⁻, prefer the O²⁻ 32*e* site.^[11] In our previous study,^[12] the DFT-optimized hexagonal cell of LTO matched best with experimental X-ray diffraction (XRD) data ($R_{wp}=6.2\%$) as compared with either the corresponding cubic ($R_{wp}=6.863\%$) or triclinic ($R_{wp}=16\%$) structures. In the hexagonal structure, every sixth layer along the *c*-axis is composed of solely Li ions. Li⁺ ions occupy all of the tetrahedral 8*a* sites and 1/6 of the octahedral 16*d* sites, whereas Ti⁴⁺ ions take up the rest of the 16*d* sites. In addition, the octahedral 16*c* vacancies provide for possible sites for subsequent Li⁺ intercalation and diffusion.

Nevertheless, for anion doping,^[11,13–20] relatively little work has been previously reported in this field as compared with cation doping,^[6,12,21,22] possibly due to the limited choices of anion dopants. Even so, this compound can be readily doped with halides, as implied by the increased number of O²⁻ sites (12) as compared with the corresponding Ti⁴⁺ (5 sites) and Li⁺ (4 sites).^[23] Moreover, as mentioned previously, based upon the band gap between the O *p*-state and the empty Ti *d*-states, substituting oxygen with other anions will induce shifts in the molecular orbital energy, thereby potentially leading to a decrease in the band gap energy. Not surprisingly, it has been previously reported that F⁻,^[13,15,16,24–28] Cl⁻,^[14] Br⁻,^[17,19,29] and N³⁻^[18,29–31] have all been successfully incorporated within LTO nanoscale motifs, such as nanosheets,^[32] nanoparticles,^[19] and nanospheres.^[27] These ions were chosen, because of their similar sizes as compared with O²⁻, so as to facilitate the substitution process.

Specifically, surface fluorination of LTO has been explored to passivate the surface of the material with Li–F moieties to effectively prevent reactions with the electrolyte and to enhance electron conductivity at the surface.^[15,20,33] This protocol resulted in an approximately 12–14% higher initial capacity and a roughly 9–10% higher Coulombic efficiency as compared with pristine LTO.^[15] A combination of Al³⁺ and F⁻ ion doping yielded better electrochemical performance than either dopant on its own, initially delivering 121 mAh g⁻¹ at 0.15 mA cm⁻².^[13] Furthermore, a previous report showed that doping of F⁻ directly into the LTO lattice delivered performance values of 101 mAh g⁻¹ at 5 A g⁻¹ with a retention of 84% of initial capacity after 1000 cycles at 2 A g⁻¹.^[16] In addition, Br⁻ ion doping of LTO has also been investigated, both structurally^[11] and electrochemically,^[18,19] the doping process improved the

electronic conductivity and the lithium diffusion rate by not only widening the lithium transport channel but also increasing the ratio of Ti³⁺/Ti⁴⁺.^[18,19] The best reversibility and cycling stability was observed with $x=0.2$ within Li₄Ti₅O_{12-x}Br_{*x*}, especially at high rates; it was noted that ≈ 100 mAh g⁻¹ could be delivered at 10C as compared with ≈ 40 mAh g⁻¹ for pristine LTO.^[19]

To the best of our knowledge, only one previous report of a Cl-doped LTO system exists in the literature.^[14] This study asserts that Cl⁻ doping promotes enhanced conductivity by favorably increasing the Ti³⁺/Ti⁴⁺ ratio.^[14,15] This high-temperature solid-state synthesis of Li₄Ti₅O_{11.8}Cl_{0.2} yielded particles in the size range of 3–8 μ m.^[14] In those experiments, at a rate of 0.5C, the Cl-LTO delivered 149 mAh g⁻¹, which was a 26% higher capacity as compared with the control. At a 2C rate, the initial capacity was 121 mAh g⁻¹, which decreased by 16% to 102 mAh g⁻¹ in the 50th cycle.

It should be emphasized that the choice of the dopant ion necessarily entails thoughtful consideration of its physical and chemical nature. For example, as compared with bromine, Cl possesses a significantly higher electronegativity value (3) as compared with Br (2.8). Moreover, as compared with the size of the oxygen anion (i.e., 140 pm), the chlorine anion (167 pm) is closer in size relative to that of the bromine anion (182 pm), but noticeably larger than that of the corresponding fluorine anion (133 pm).^[6] All of these variables imply that both Cl and F can more readily spatially dope into the underlying LTO lattice as compared with bromine. In addition, Cl is the more desirable option as compared with F, because whereas use of Cl induces a favorable increase in the ratio of Ti³⁺/Ti⁴⁺ to improve the conductivity of the underlying LTO, by contrast, employing F may generate the creation of an unfavorable, passivating Li–F layer.

In a series of experiments, we have synthesized hierarchical LTO motifs (Figure S1 in Supporting Information), that have been subsequently doped with both F and Cl dopants.^[12] However, in recognition of the practical reality that the results of our Cl anion dopant work were far more reproducible and reliable than its F counterpart, we have focused exclusively on describing our Cl studies within the main text. Our extensive, analogous F data on variously produced LTO motifs are described in detail both within the main text and Supporting Information sections (Figures S2–S4). However, we found it to be extremely challenging to precisely quantify the amount of F dopants within our as-prepared samples. Hence, we concluded that it was more prudent to avoid drawing any durable, dependable conclusions about electrochemical activity.

Therefore, the novelty of our current contribution is several-fold. First, from the perspective of structure-property correlations, we have emphasized herein the benefits of a hierarchical three-dimensional (3D) morphology for electrochemical performance, including but not limited to 1) an increased surface area, 2) reduced Li-ion diffusion distances, and 3) increased cyclability.^[12] We synthesized a range of Cl-doped materials to explore the physical and chemical implications of increased Cl dopant quantities on the corresponding LTO structure. Second, we have made important synthetic advances in enabling the

large-scale, efficient, and solution-based production of the 3D architectures. In particular, we used not only 1) H₂O₂ as a chemical etching agent and a reliable means of modulating morphology but also 2) titanium butoxide (TBOT) liquid precursor in lieu of a solid Ti foil to facilitate a more rapid and effective reaction. Third, theory has been employed to describe the nature of the Cl based dopant. Based upon an underlying hexagonal LTO structure, all the possible sites for chlorine anion doping (referred to hereafter as Cl-doping) at the content of 0.5 in Li₄Ti₅O_{11.5}Cl_{0.5} and its corresponding effects upon electrochemical activity have been probed using DFT calculations. Fourth, electrochemical characterization of the material response was assessed using cyclic voltammetry and electrochemical impedance spectroscopy and evaluated at various rates and over extended cycling regimes.

Experimental Section

Synthesis

Hydrothermal Synthesis of Precursor Li₄Ti₅O₁₂ Nanoflowers: The protocol used herein was based upon and optimized from a previously reported method.^[34,35] Initially, 50 mL of water was placed within a 120 mL autoclave, followed by the addition of 0.80 g of LiOH (Acros Organics, 98%). The mixture was then stirred until complete dissolution was achieved. Subsequently, 2.5 mL of 30% (w/w) H₂O₂ (VWR) aqueous solution was added in dropwise, followed by strong stirring at room temperature for 5 min. After that, 1.7 mL (i.e., 5 mmol) titanium butoxide (TBOT) (Acros Organics, 99% or Alfa Aesar 99+%) was introduced dropwise and stirred for 3 hours. As a clarifying note, based on these commercial purity levels reported, hereafter, we will refer to these as-obtained Acros Organic and Alfa Aesar chemicals as 'lower grade' and higher grade' titanium-based precursors, respectively. The solution was then placed within a steel autoclave and a hydrothermal reaction was initiated for 36 hours at 130 °C. The as-formed white precipitate product was washed with anhydrous ethanol 3 times, prior to a final annealing step within a tube furnace at 500 °C for 3 hours using a ramp rate set at 3 °C per minute.

Hydrothermal Synthesis of Cl-doped Li₄Ti₅O₁₂ Nanoflowers: A precursor solution of 5 M NH₄Cl (Alfa Aesar, 98+%) was prepared. To create 0.5 mmol Cl-doped LTO (Cl-LTO), ≈0.1 mL of the solution was added in, following the introduction of H₂O₂, but prior to the addition of TBOT. For the higher-doped 5 mmol Cl-LTO sample, instead of ≈0.1 mL, ≈1 mL of the solution was put in, following the same protocol.

Characterization techniques and methodology

XRD: LTO and relevant Cl-LTO samples were prepared by dispersion of the nanomaterial in ethanol and then drop-casting that mixture several times onto a zero-background holder (MTI Corporation, zero diffraction plate for XRD, B-doped, p-type Si, measuring 23.6 mm in diameter by 2 mm in thickness). Diffraction pattern data were then obtained on a Rigaku Miniflex diffractometer, operating in the Bragg configuration. The results were separately collected using Cu_{Kα1} irradiation (λ = 1.54 Å) across the range of (i) 10° to 80° with a scanning rate at 5° min⁻¹ and (ii) 5 to 90° with a step size of 0.05° at a speed of 5° min⁻¹.

SEM imaging: An ultra-high-resolution field emission Hitachi 4800 scanning electron microscopy was employed to characterize the

apparent morphology of as-prepared structures. Specifically, the pristine and Cl-LTO samples were generated by initially dispersing the targeted nanomaterial in ethanol and then drop casting aliquots onto a silicon wafer.

TEM Imaging: To characterize structure/morphology and chemical composition, we collected relevant images and Energy-Dispersive X-ray Spectroscopy (EDS) measurements, respectively. Specifically, the data were acquired using a JEOL 1400 transmission electron microscope (TEM) with EDS mapping capabilities, equipped with a 2048 × 2048 Gatan CCD camera and operated at an accelerating voltage of 12 kV. Samples were prepared by dispersing the powder samples in ethanol coupled with subsequent drop-casting onto a lacey carbon-coated copper grid.

X-ray photoelectron spectroscopy (XPS): X-ray photoelectron spectroscopy was used to confirm elemental composition and derive oxidation state information for the different elements within our samples. We used a procedure similar to that utilized to produce SEM samples. Specifically, product powders were dispersed in ethanol and then drop cast onto an underlying Si wafer (1 cm × 1 cm). XPS experiments were conducted using a home-made system, with a model SPECS Phoibos 100 electron energy analyzer for electron detection. As the X-ray source, Al_{Kα} radiation (1486.6 eV) (model XR 50) was utilized during the data collection algorithm. Spectra associated with the Ti 2p and Cl 2p regions were processed and corrected using a Shirley background.

Density functional theory: DFT was implemented using the Vienna ab initio simulation package (VASP).^[36,37] Specifically, the spin-polarized DFT+U calculations^[38–40] were carried out with the Projector augmented-wave (PAW) potential^[37,41] using the Perdew–Burke–Ernzerhof (PBE) exchange–correlation functional,^[42] and a kinetic energy cutoff of 580 eV. A Hubbard *U* correction of 4.5 eV was applied to the Ti d-orbitals, following our previous study.^[12] The Gaussian smearing method was used with the total energies converging better than 10⁻⁵ eV, with the final force on each atom set to be less than 0.02 eV Å⁻¹. The first Brillouin zone was sampled using a 7 × 7 × 5 k-mesh. The pristine Li₄Ti₅O₁₂ crystal structure was modeled using a hexagonal cell containing two formula units.^[43] The DFT-optimized lattice parameter (8.46 Å) was in reasonable agreement with the value measured experimentally (8.35 Å).^[44]

To determine the nature of the occupancy of the Cl dopants, several possible sites were considered. Only the most stable configuration was chosen from the DFT calculations for subsequent fitting to the measured XRD patterns and lithiation performance results. Considering an overall process of (Li₄Ti₅O₁₂)₂ + Cl → (Li₄Ti₅O_{11.5}Cl_{0.5})₂ + O, various Cl-doping sites were tested, and the corresponding formation energies were calculated as noted by Equation (1):

$$E_f = E_{(\text{Li}_4\text{Ti}_5\text{O}_{11.5}\text{Cl}_{0.5})_2} - E_{(\text{Li}_4\text{Ti}_5\text{O}_{12})_2} + E_o - E_{\text{Cl}} \quad (1)$$

wherein *E* is the DFT calculated total energy in eV of a specific configuration, whereas *E*_o and *E*_{Cl} are equal to the total energy of free O and Cl in gas phase, respectively.

The average intercalation voltage was calculated using Equation (2):^[45]

$$V = \frac{E_{\text{Li}_{4+x}\text{Ti}_5\text{O}_{12}} - E_{\text{Li}_4\text{Ti}_5\text{O}_{12}} - xE_{\text{Li}}}{xF} \quad (2)$$

wherein *x* is the degree of lithiation. *E*_{Li} is the total energy of bulk metallic Li in eV. *F* is Faraday's constant.

Electrochemistry: A mixture of either 85% as-prepared lithium titanate (LTO) or Cl-LTO, 5% carbon, 5% graphite, and 5% polyvinylidene fluoride (PVDF) was cast onto an aluminum foil. The electrolyte used was 1 M LiPF₆ in ethylene carbonate/dimethyl carbonate (3:7 by volume). Coin-type cells were assembled within an argon filled glovebox using a polypropylene separator and Li metal foil. For all electrochemical testing, the theoretical capacity used for the determination of C-rates was 175 mAhg⁻¹. Two sets of cells were cycled using a series of rates, either (1) 0.2, 20, 40, 0.2C or (2) 0.2, 2, 5, 10, 0.2 over a voltage window of 1.0–2.5 V.

Galvanostatic cycling was performed over a voltage window of 1.0–2.5 V for 100 cycles at a 2C rate using cells that had already undergone rate capability tests. Cyclic voltammetry (CV) measurements were collected in the voltage window of 1.0–3.0 V at scan rates of 0.5, 1.0, 2.0, 4.0, and 5.0 mVs⁻¹, respectively. Electrochemical impedance spectroscopy (EIS) was measured both before and after all the electrochemical tests using a BioLogic VSP impedance analyzer with an amplitude of 10 mV over a frequency range of 100 kHz to 10 mHz. The impedance data, after cycling, were fit using ZView from SAI Software.

Results and Discussion

Insights into synthesis and growth mechanism

Our crucial synthetic modification was to increase the sample yield by substituting the Ti foils (used in our original published protocol^[12]) with a solution-based Ti precursor, namely, TBOT. Why the need to alter an ostensibly effective synthesis procedure? In effect, with our original process, we found in our preliminary experiments, that despite the potential for successful Cl doping, we could neither (a) properly control the amount of Cl doping nor (b) ensure uniform, homogeneous LTO purity at the scale of 500 mg, needed to run the electrochemical measurements. However, the relationship among the initial versus incorporated dopant concentrations was neither exactly proportional nor correlative. We traced all of these issues in part to the use of a solid Ti sheet foil as a precursor, which understandably was not as readily dispersible in solution as fine, granular powder and hence was less reliable in terms of consistently exposing a reproducible surface area of Ti to subsequent reaction with H₂O₂. Therefore, the switch from utilizing Ti foil to TBOT as the Ti precursor led to improved sample consistency with the potential for generating functionally relevant amounts of pure sample. The resulting consequences of doing so were that we could not only (a) control precursor purity to a much greater extent but also (b) increase overall product yields to an unprecedented degree. Significantly, the yield rose from an initial 40 mg per run using the Ti foil precursor to ≈450 mg per run using TBOT as the liquid-based precursor.

Indeed, altering the precursor led to changes in the overall reaction time/temperature associated with both the hydrothermal and annealing conditions. Our optimized synthesis protocol herein was based on prior literature. However, as opposed to stirring for 30 minutes and hydrothermally heating for 4 hours as with the original procedure, our current methodology involves stirring of the solution for 3 hours followed by a hydrothermal heat treatment for 36 hours. This was performed at an initial concentration of 0.5 M LiOH in a 5:1 Li: Ti ratio,

while decreasing the amount of H₂O₂ from 7.83 to 2.5 mL, as described in our reported synthesis.^[46]

It is worth noting that H₂O₂ used in our current synthesis not only enabled the formation of the desired morphology, but also provided for a reliable means for controlling the rate of hydrolysis of TBOT upon its addition to the aqueous LiOH solution. This latter attribute was crucial, because it meant that TiO₂ impurities, which might have rapidly formed when the TBOT precursor was exposed to oxygen in either air or water, were successfully minimized. Nevertheless, this 5:1 Li: Ti ratio yielded Li₂TiO₃ impurities (situated at 21° in the associated XRD pattern), likely due to an excess quantity of LiOH in solution (Figure 1 A, red). Therefore, the effects of altering discrete experimental parameters, such as precursor concentrations and TBOT purity, were analyzed in order to optimize the synthesis of as-prepared Li₄Ti₅O₁₂ nanoflowers.

A. Effect of lithium concentration.

Specifically, we explored the effects of varying molarities from 0.4 to 0.5 M LiOH in 0.02 M increments (Figure 1 A) with a fixed amount of the Ti precursor (1.7 mL TBOT, 99% purity, 5 mmol). It was observed that at 0.42 M (Figure 1 A, blue), there was still a slight Li₂TiO₃ impurity, arising from perhaps an excess of LiOH. Conversely, at 0.4 M (Figure 1 A, pink), we noted a rising level of TiO₂ impurity (≈25°), likely resulting from insufficient quantities of LiOH. Therefore, we postulated an optimized LiOH molarity of 0.41 M LiOH, indicative of a 4.1 Li: 1 Ti ratio. The resulting morphology was confirmed by SEM to consist of nanoflower motifs with an average diameter of ≈1 μm (Figure 1 B).

B. Effect of titanium butoxide precursor amount

As the amount of TBOT was significantly lower than the corresponding amount of Li, we also explored a complementary set of experiments in which we systematically varied Ti precursor quantities. As stated above, our preliminary experiments centered on a 5: 1 Li: Ti precursor ratio. Subsequently, we synthesized samples both below and above this initial ratio. In particular, we ran experiments with Li: Ti ratios of 1) 7: 1 (i.e., a relative increase in LiOH amount) and 2) 4: 1 (i.e., relative reduction in LiOH quantity), respectively. The XRD patterns of the resulting samples are presented in Figure S5 (Supporting Information). We determined that the sample incorporating a 7: 1 Li: Ti ratio (Figure S5, blue) evinced Li₂TiO₃ impurities, whereas the corresponding 4: 1 Li: Ti ratio sample (Figure S5, green) showed the presence of TiO₂ anatase peaks, indicating that there had been too much TBOT, initially. Therefore, consistent with our results in terms of varying lithium concentration (Section A), the optimized Li: Ti ratio was 4.1:1, as observed in Figure 1.

C. Effect of titanium butoxide purity.

Moreover, the morphology of the resulting 3D nanoflower structures was maintained, even when switching the precursor

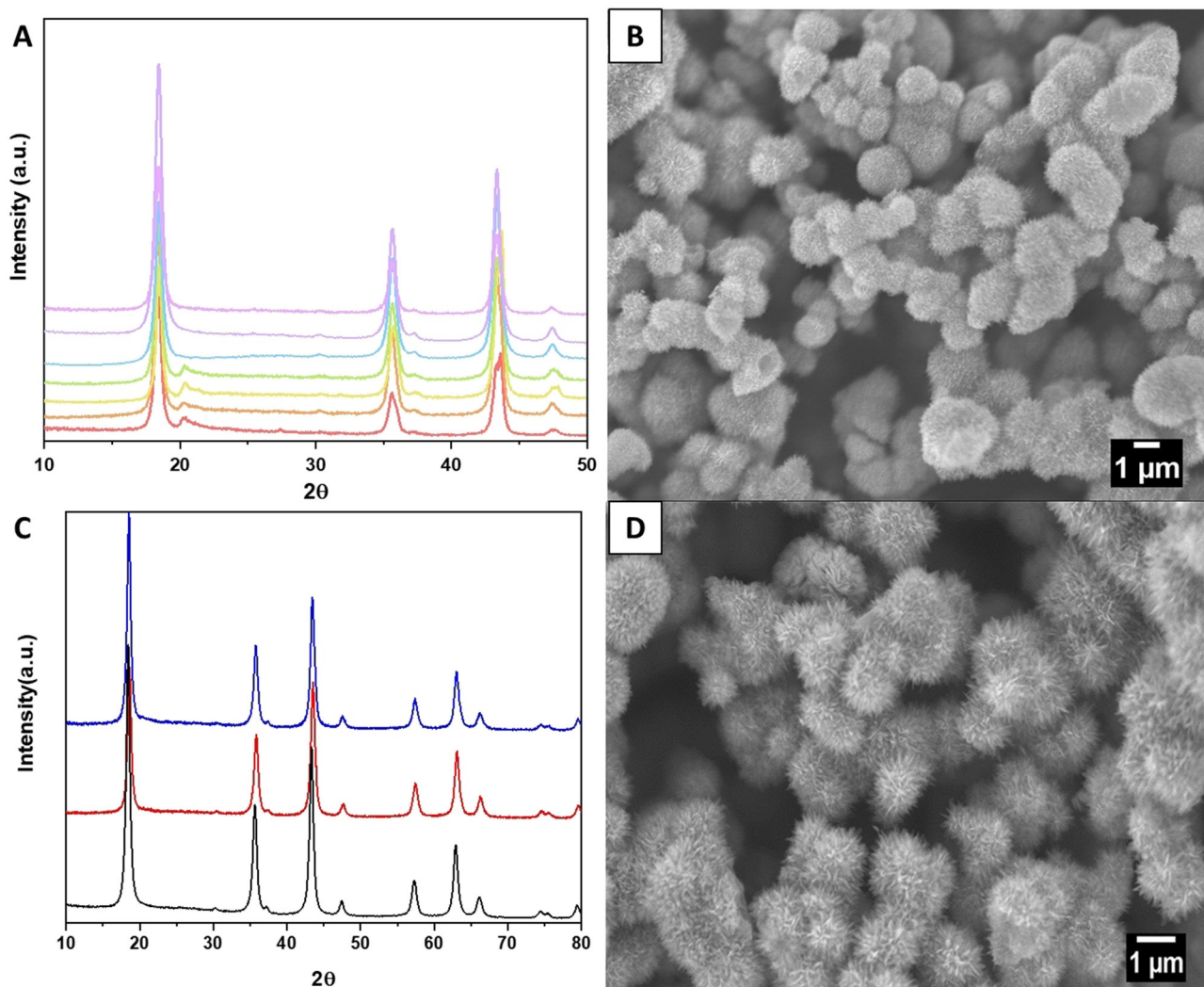


Figure 1. (A) XRD patterns of LTO synthesized using varying LiOH concentrations from 0.5 M (red), 0.48 M (orange), 0.46 M (yellow), 0.44 M (green), 0.42 M (blue), 0.41 M (purple) and 0.40 M (pink). The corresponding (B) SEM image of LTO synthesized at 0.41 M LiOH is shown. (C) XRD patterns of LTO created with (i) a lower purity TBOT precursor with 0.41 M LiOH (black), (ii) a higher purity TBOT precursor with 0.40 M LiOH (red), and (iii) a higher purity TBOT precursor with 0.42 M LiOH (blue). The corresponding (D) SEM image of LTO synthesized with the higher purity TBOT precursor coupled with 0.40 M LiOH is presented.

from Ti to TBOT. Specifically, initial samples in Sections A and B were synthesized using titanium butoxide (TBOT) with a designated purity level of 99%.

We then explored the effects of increasing TBOT purity on sample formation. Specifically, we ran the synthesis using a higher grade of TBOT precursor (HP-TBOT), which was reported to contain a purity level of 99+%. The results of these experiments are shown, using HP-TBOT with a LiOH solution concentration set at 0.40 M (Figure 1C, red) and 0.42 M (Figure 1C, blue), respectively. By means of comparison, pristine LTO nanoflowers synthesized using a 0.41 M LiOH concentration (Figure 1C, black) with the original TBOT precursor are also highlighted. Whereas the 0.42 M LiOH HP-TBOT sample gave rise to a slight Li_2TiO_3 impurity, the corresponding 0.40 M LiOH HP-TBOT sample yielded pure LTO with increased crystallinity, as compared with the analogous sample, created using standard purity TBOT. As such, the use of a higher purity precursor (i.e., HP-TBOT) not only led to a greater crystallinity but also a supe-

rior purity (i.e., absence of Li_2TiO_3 impurity peaks), as compared with samples prepared with standard purity TBOT.

Because the amounts of TBOT and LiOH precursors are necessarily coupled and interdependent in generating the desired LTO material without any detectable impurities, we were finally able to optimize reagent conditions, such that a pure product could be ultimately generated with 0.40 M LiOH using HP-TBOT with an experimentally achievable 20 Li : 5 Ti mmol ratio. The corresponding SEM images of this sample were acquired (Figure 1D), and our data corroborate formation of a nanoflower morphology, measuring $\approx 1 \mu\text{m}$ in diameter.

D. Effect of hydrothermal reaction time

Furthermore, the effect of varying the hydrothermal reaction time was also explored. Specifically, LTO systems synthesized hydrothermally at 4 h and 12 h were investigated using XRD. The resulting isolated compositions after 4 h (Figure S5, red) and 12 h (Figure S5, black) of reaction imply formation of TiO_2

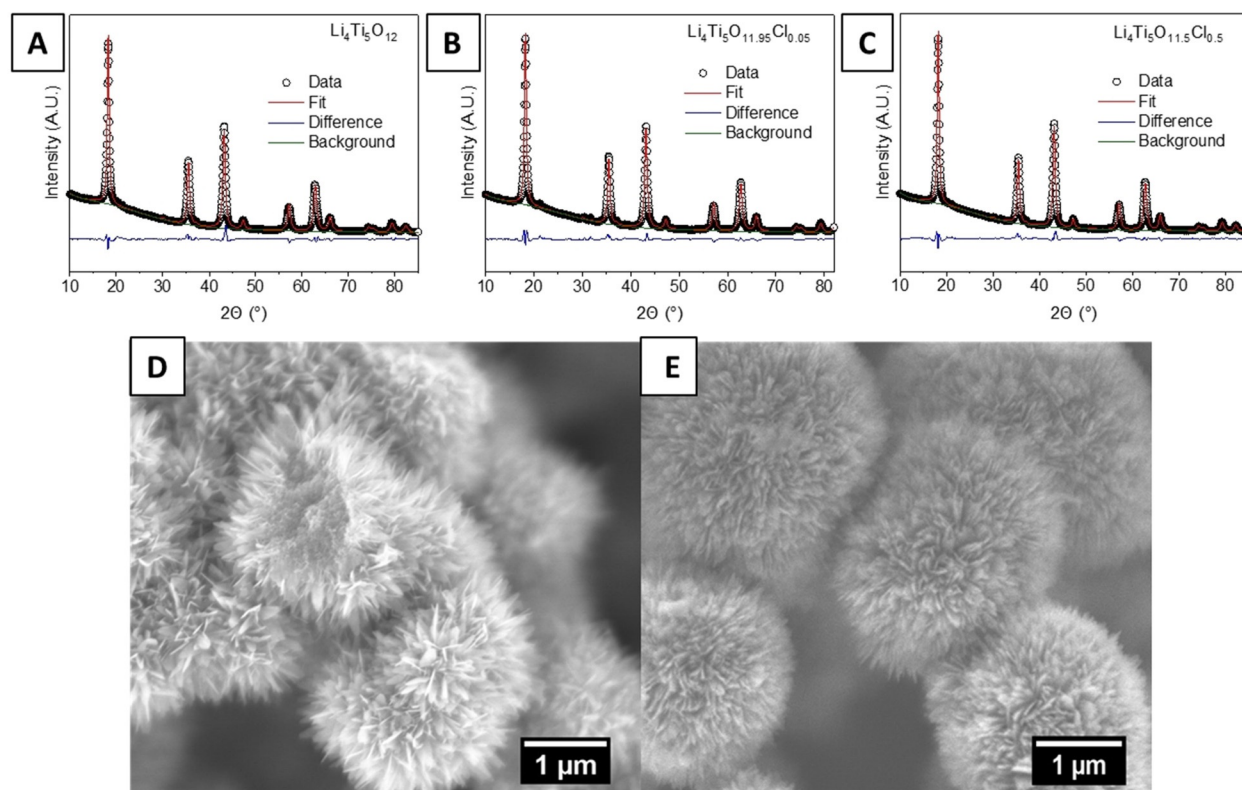


Figure 2. XRD patterns and Rietveld refinements of (A) pristine LTO ($\text{Li}_4\text{Ti}_5\text{O}_{12}$), (B) 0.5 mmol Cl-LTO ($\text{Li}_4\text{Ti}_5\text{O}_{11.95}\text{Cl}_{0.05}$), and (C) 5 mmol Cl-LTO ($\text{Li}_4\text{Ti}_5\text{O}_{11.5}\text{Cl}_{0.5}$) samples, using the $Fd\bar{3}m$ structure. The corresponding SEM images of (D) the 0.5 mmol LTO-Cl and (E) the 5 mmol LTO-Cl samples are also shown.

impurities, likely emanating from an incomplete conversion process. These findings are consistent with previous reports of a similar synthesis.^[34] Therefore, the optimized reaction conditions implied 1) a hydrothermal time of 36 h and 2) a precursor ratio of Li: Ti of 4: 1, in which we 3) used HP-TBOT coupled with LiOH at a concentration of 0.40 M.

E. Characterization of Cl-LTO samples

Even more importantly for our series of experiments, we discovered that our new synthetic procedure enabled a more stoichiometric approach to determining overall dopant ion incorporation. In particular, while still imperfect, nevertheless, the amount of precursor Cl dopant correlated much more closely with the quantity of actual anionic uptake in the final product as compared with our initial synthetic protocol. Specifically, two Cl-doped samples were synthesized for this experiment using the optimized reaction conditions described above.

To introduce the desired dopants and probe the effect of dopant levels in general, we utilized 0.5 mmol and 5 mmol, respectively, of the Cl-containing dopant, NH_4Cl . Specifically, NH_4Cl was utilized as opposed to LiCl so as not to unnecessarily increase the amount of Li^+ ions, which might have yielded unwanted Li_2TiO_3 impurities. The addition of anionic dopants was a facile process, as it involved simply adding in a pre-determined amount of an aqueous solution of the desired ammonium salt, that is, NH_4Cl , after adding in the H_2O_2 into the reaction medium. From these runs, the resulting dopant molar

amounts were determined to be consistent with the desired formulae of $\text{Li}_4\text{Ti}_5\text{O}_{11.95}\text{Cl}_{0.05}$ and $\text{Li}_4\text{Ti}_5\text{O}_{11.5}\text{Cl}_{0.5}$, respectively.

The XRD patterns taken for each of the anionic-doped samples are consistent with the pristine LTO sample (Figure 2A), evincing no apparent change in the structure of the LTO as a function of doping (Figure 2B and C). All diffraction data matched well with a cubic spinel structure with the $Fd\bar{3}m$ space group (PDF#00-049-0207). Rietveld refinement was performed on the XRD patterns for the pristine 0.5 mmol Cl-doped LTO, and 5 mmol Cl-LTO samples, respectively. Atomic positions for each of these analyzed materials can be found in Table S1. The lattice parameter shifted slightly from 8.3508 to 8.3588 Å and onwards to 8.3553 Å for the pristine, 0.5 mmol Cl-LTO, and 5 mmol Cl-LTO samples, respectively (Table S2). Lattice parameter expansion to this degree has been previously noted for Br-doped LTO, and was attributed to the larger ionic radius of the dopant ion as compared with the O^{2-} ion.^[18] For all samples, the crystallite size was ≈ 28 nm. No additional phases, such as Li_2TiO_3 , were evident, based on the refinement. Moreover, associated SEM images corroborated our expectation that the presence of the dopants did not substantively impact upon the LTO morphology (Figure 2D and E).

To ascertain chemical composition, X-ray photoelectron spectroscopy (XPS) was utilized to validate the degree of successful doping of Cl within the underlying LTO matrix. The experimental data are shown in black, and the corresponding fitting curves are denoted by a dotted green line in both Figure 3A and 3B. The Ti 2p region (Figure 3A) is shown for pris-

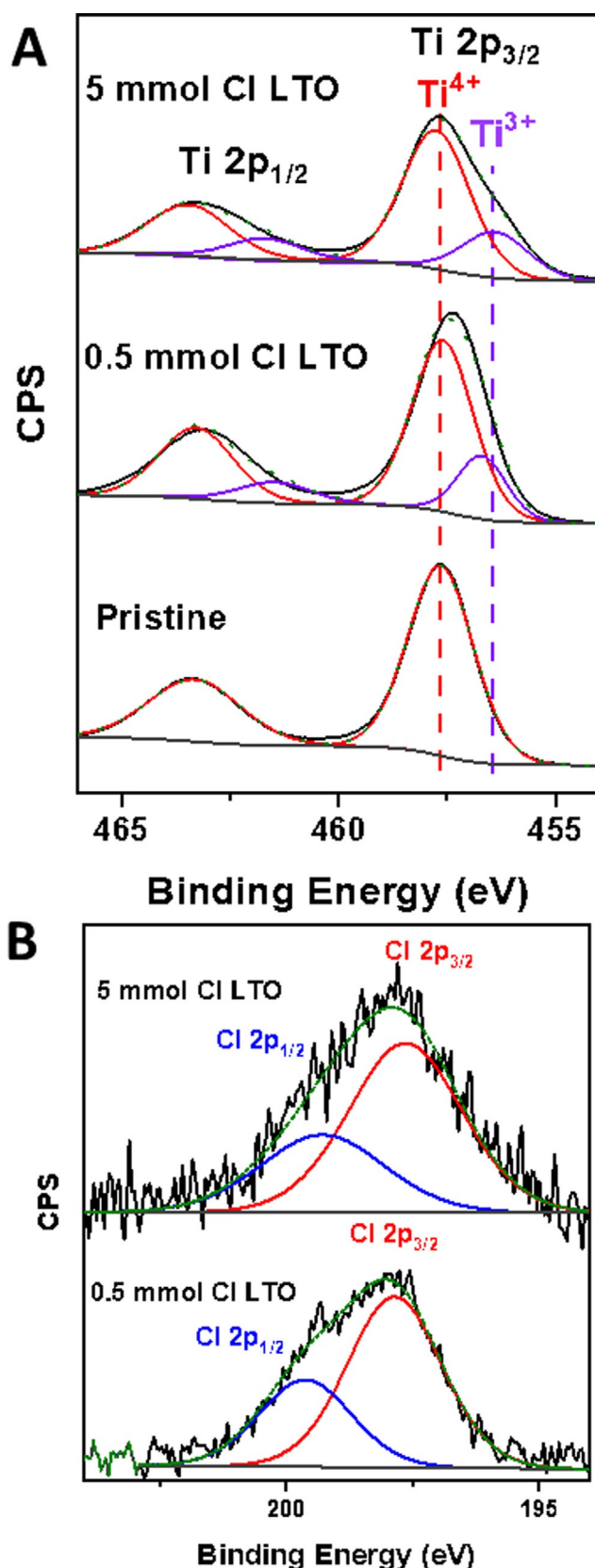


Figure 3. XPS spectra of (A) the Ti 2p region of pristine LTO (bottom panel), 0.5 mmol Cl-LTO (middle panel), and 5 mmol Cl-LTO (top panel), respectively. XPS spectra of (B) the Cl 2p region of the 0.5 mmol Cl-LTO (bottom panel) and 5 mmol Cl-LTO (top panel) samples.

tine LTO (bottom panel), 0.5 mmol Cl-LTO (middle panel), and 5 mmol Cl-LTO (top panel) samples. Specifically, the pristine LTO sample highlights peaks for the Ti 2p_{1/2} and Ti 2p_{3/2} regions at 463.3 (blue) and 457.7 eV (red), respectively, consistent with the Ti⁴⁺ oxidation state associated with LTO formation (Figure 3A, Table 1). These values also corroborate previously reported data in the literature.

For 0.5 mmol Cl-LTO, the corresponding sample exhibits a slight negative shift for the Ti 2p_{1/2} and Ti 2p_{3/2} peaks related to Ti⁴⁺ peaks. Indeed, the collective presence of peak signals situated at 463.2, 461.6, 457.5, and 456.5 eV respectively, are indicative not only of Ti⁴⁺ but also of Ti³⁺, the latter of which is known to increase conductivity. Furthermore, signals attributable to Ti³⁺ and Ti⁴⁺ are further highlighted by the purple and red dashed lines, respectively. Because the presence of Ti³⁺ is clearly indicated by the purple dashed line, we can convincingly assert that our data confirm the presence of Cl insertion within the underlying LTO matrix (Figure 3A middle panel, Table 1). The Cl 2p peaks for this sample signify 2p_{1/2} and 2p_{3/2} peaks, located at 199.6 and 197.8 eV, respectively (Figure 3B, Table 1). These results are consistent not only with the presence of Cl within the LTO matrix but also Ti³⁺ formation, since analogous data have been observed upon anionic doping within LTO.^[14,15]

The analogous 5 mmol Cl-LTO sample also gave rise to not only Ti⁴⁺ 2p peaks at 463.7 and 457.6 eV, but also Ti³⁺ signals at 461.2 and 456.1 eV, corresponding to the 2p_{1/2} and 2p_{3/2} peaks, respectively (Figure 3A top panel, Table 1). The Cl 2p peaks, situated at 199.3 and 197.6 eV, are associated with the 2p_{1/2} and 2p_{3/2} peaks for the 5 mmol Cl-LTO sample. When comparing the Ti⁴⁺: Ti³⁺ ratio between the 0.5 mmol Cl-LTO and its 5 mmol Cl-LTO counterpart, we found that the 0.5 mmol Cl-LTO sample highlighted a measured ratio of Ti⁴⁺: Ti³⁺ of 3.4: 1, which is within experimental error of the corresponding 3.0: 1 ratio calculated for the analogous 5 mmol Cl-LTO sample (Table 1). Overall, these results are consistent with essentially similar levels of Cl doping within the LTO for both samples. This observation could most likely be ascribed to the idea of a threshold level of doping, wherein an excess of Cl would result in the formation of LiCl, which is soluble in water and therefore, most likely washed out during subsequent sample processing. One practical consequence is that the concentration of Ti³⁺ detected is not necessarily linearly proportional to the quantity of the Cl dopant amount introduced into the LTO system.

Therefore, we concluded that the 0.5 mmol Cl-LTO sample incorporated an 'optimized' and sufficient amount of Cl doping and that it was wise to assess the effect of Cl doping by comparing the electrochemical performance of that material versus that of the pristine LTO control. We note that to bolster the XPS data, TEM-EDS mapping analysis of the 0.5 mmol Cl-LTO sample substantiated the presence of a homogeneous dispersion of Cl (Figure 4) within these highly crystalline nanoflower motifs, as previously verified by a combination of XRD and SEM.

Table 1. Summary of Relevant XPS Spectra.

Sample	Ti ⁴⁺ 2p _{1/2} [eV]	Ti ³⁺ 2p _{1/2} [eV]	Ti ⁴⁺ 2p _{3/2} [eV]	Ti ³⁺ 2p _{3/2} [eV]	Cl 2p _{1/2} [eV]	Cl 2p _{3/2} [eV]	Calculated Ti ⁴⁺ : Ti ³⁺ Ratio Detected
pristine LTO	463.3	N/A	457.6	N/A	N/A	N/A	NA
0.5 Cl-LTO	463.2	461.6	457.5	456.5	199.6	197.9	3.4: 1.0
5Cl-LTO	463.7	461.2	457.6	456.1	199.3	197.6	3.0: 1.0

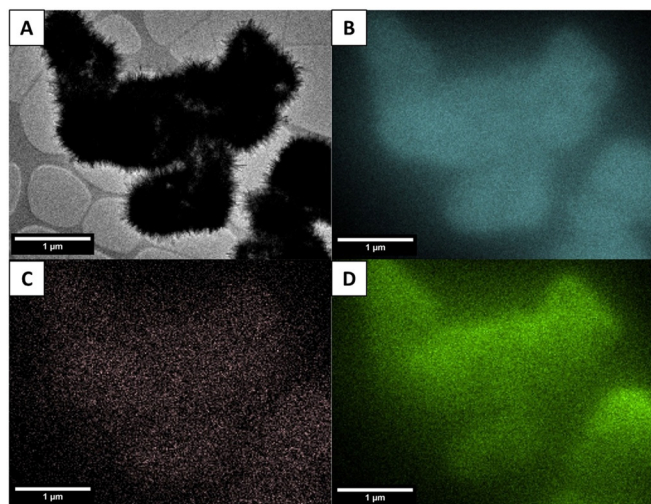


Figure 4. (A) TEM image of the 0.5 mmol Cl-LTO sample. Representative elemental EDS mapping of the region associated with Cl-LTO nanoflowers, highlighting the chemical spatial distribution of (B) Ti, (C) O, and (D) Cl. Scale bars are 1 micron in each image.

F. Complementary studies of F-doped LTO using TBOT as the Ti precursor

By analogy with the Cl-doping work, fluorine doping of LTO nanoflowers (F-LTO) was also explored, due to similar arguments about potentially enhancing electronic conductivity.^[15,16,26–28] As observed in Figure S4A (Supporting Information), XRD patterns of F-doping using 0.5 mmol (red) and 5 mmol (blue) of the respective NH₄F salts are consistent with an underlying Li₄Ti₅O₁₂ structure (black). However, whereas the 0.5 mmol F-LTO sample yielded pure LTO, the 5 mmol F-LTO sample evinced high amounts of an LiF impurity, indicating that the F dopant amount was likely present in unacceptable excess. Nevertheless, as a promising result, SEM imaging of the 0.5 mmol F-LTO sample (Figure S4B) suggested that F-doping of the LTO nanoflower sample did not apparently degrade either its intrinsic 3D morphology or its inherent 1–3 µm dimensions.

What was more problematic emanated from XPS characterization of the 0.5 mmol F-LTO sample. Data are shown for the Ti 2p region (Figure S4C) and the F 1s region (Figure S4D) respectively. For the Ti 2p region, only Ti⁴⁺ was apparent, implying that despite F-doping, Ti³⁺ did not form. This observation is consistent with previous reports of F-doping of LTO,^[15] wherein doping of F within LTO actually led to LiF formation; in those experiments, the fluorinated surface of LTO acted as electron trapping sites and reduced interfacial electron trans-

fer, thereby leading to less electrochemically active surfaces. Hence, our cumulative synthesis and characterization data suggested that the 0.5 mmol Cl-LTO sample was the most promising one to test for its electrochemical performance, since it was not only pure, but also possessed favorable Ti³⁺ species.

Theoretical studies

A. Cl-Doping effect—atomic structure:

As mentioned, Cl-LTO was studied to elucidate the doping-induced effect upon the corresponding intrinsic structures and properties of LTO. Based upon an underlying hexagonal LTO structure (Figure 5A), all of the possible sites for Cl-doping with the content of 0.5 within Li₄Ti₅O_{11.5}Cl_{0.5} were tested using DFT calculations. Our results highlight that the Cl⁻ ion prefers to substitute for the O²⁻ ion at the octahedral 32e site at the corner shared by Li 8a, Li 16d and two Ti 16d ions (Figure 5B), in agreement with a prior report.^[11] However, this substitution is energetically unfavorable with an energy loss of 1.85 eV based on the calculated formation energy, which also agrees with previous literature.^[11] Furthermore, the cell volume expansion with respect to pristine LTO, is 2.75% after doping in with Cl in a process, which is likely to facilitate Li diffusion by the expansion of channels within the LTO lattice.

B. Cl-Doping effect—electronic structure:

In addition to evident atomic structure effects, significant changes in the electronic signature of LTO due to Cl-doping were also observed. According to our calculated projected density of states (PDOS) in Figure 6A, the band gap of LTO is 2.10 eV, which is within the range of previous reported experimental and calculated values.^[9] These results confirm that LTO is a typical insulator with low electronic conductivity. In pristine LTO, the valence bands were mainly composed of O 2p states, whereas the conduction bands were dominated by Ti 3d states. The significant overlap between the Ti 3d and O 2p orbitals in terms of their electronic density of states suggested a strong Ti–O interaction mediated by the TiO₆ octahedral unit.

After Cl-doping, a new intermediate Ti 3d state near the Fermi level emerged, and the band gap was significantly decreased to 0.83 eV (Figure 6B), thereby indicating that the electronic conductivity was enhanced. The position of the Fermi level (0 eV) shifts upward and reaches the newly generated intermediate state. Meanwhile, the position of all of the electronic DOS shifts downwards, consistent with n-type doping.^[47] The substitution of the O²⁻ ion with the Cl⁻ ion induces the partial reduction of Ti⁴⁺ ions (Ti6, Ti8 as shown in Figure 5B). Two Ti⁴⁺ ions, which were directly bonded to the doped Cl⁻

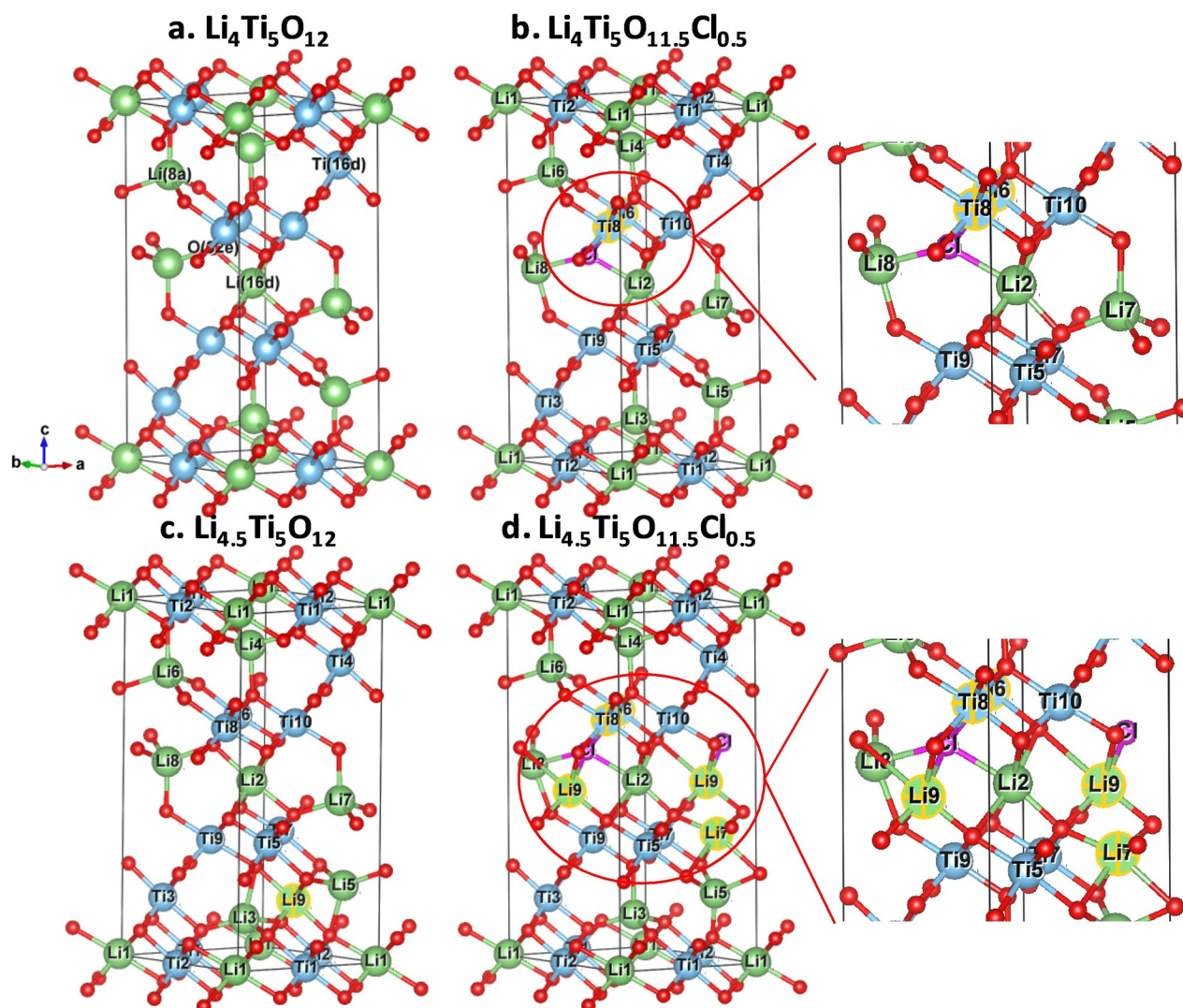


Figure 5. DFT-optimized structures of (a) a pristine hexagonal ($\text{Li}_4\text{Ti}_5\text{O}_{12}$)₂ cell, (b) a ($\text{Li}_4\text{Ti}_5\text{O}_{11.5}\text{Cl}_{0.5}$)₂ cell with Cl localized at the octahedral 32e site, (c) a lithiated ($\text{Li}_{4.5}\text{Ti}_5\text{O}_{12}$)₂ cell, and (d) a lithiated ($\text{Li}_{4.5}\text{Ti}_5\text{O}_{11.5}\text{Cl}_{0.5}$)₂ cell with Cl localized at the octahedral 32e site (Green: Li; Blue: Ti; red: O; Pink: Cl).

ion, gave rise to an intermediate state at the Fermi level. Hence, as we have experimentally observed with XPS, Ti^{4+} and Ti^{3+} ions do co-exist within the Cl-LTO species. The presence of reduced Ti^{3+} ions likely increases the observed electronic conductivity. Moreover, in the range of 0–6 eV, the increased mixing of t_{2g} and e_g orbitals indicates a slight distortion of the TiO_6 octahedra, a phenomenon also observed with Br-doped LTO.^[11]

C. Cl-Doping Effect—lithiation voltage:

To determine the doping effect on the lithiation voltage, a Li^+ ion was inserted into the 16c vacancy in both pristine LTO and Cl-LTO. In pristine LTO, the lithiation process is exothermic with the average voltage of 1.32 V and a slight volume expansion of 1.09% (Figure 5C), in agreement with previous DFT calculations.^[44,48] Cl-doping rendered the lithiation process more feasible, with an increased voltage of 1.57 V, also in agreement with previous research.^[11] The Cl^- dopant activates the adja-

cent octahedral 16c vacancy. Therefore, the intercalated Li^+ ion (Li9 as shown in Figure 5D) was directly bonded to the Cl^- ion. Upon Li intercalation, a neighboring Li^+ ion (Li7 as shown in Figure 5D) migrated from the tetrahedral 8a site to the octahedral 16c site, either spontaneously or as a result of a low barrier, due to the strong electrostatic repulsion from the intercalated Li^+ ion. The cell volume expansion with respect to Cl-LTO is 1.48% after Li insertion, which is slightly higher than the cell volume expansion measured in pristine LTO.

Electrochemistry

Cyclic voltammetry was performed on cells containing pristine LTO and Cl-LTO electrodes in a voltage range of 1–3 V at scan rates of 0.5, 1, 2, 4, and 5 mVs^{-1} , respectively (Figures 7A–B). The linear fit of the peak current (i_p) versus the square root of the scan rate for each sample is shown in Figures 7C–D. Correlation coefficients for the anodic and cathodic fits were 0.997 and 0.991, respectively, for both the pristine and Cl-LTO sam-

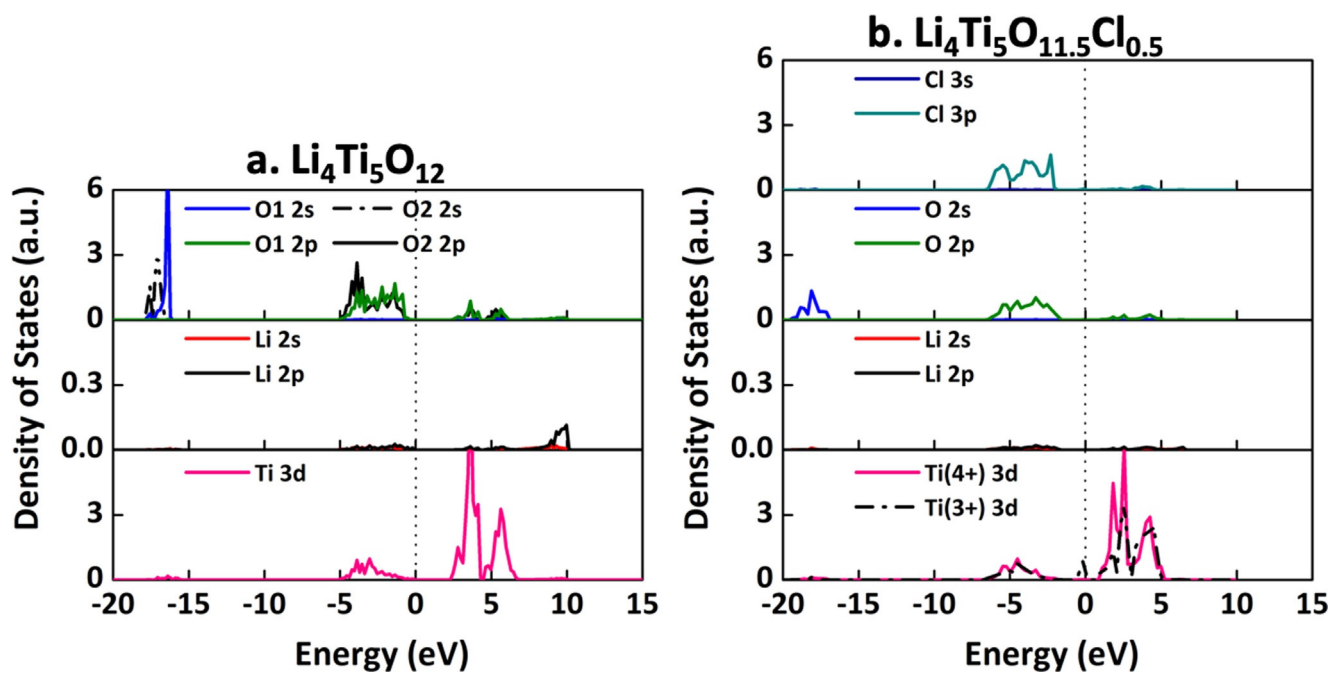


Figure 6. Projected electronic density of states (PDOS) of (a) pristine LTO and (b) $\text{Li}_4\text{Ti}_5\text{O}_{11.5}\text{Cl}_{0.5}$, with Cl localized at the octahedral 32e site.

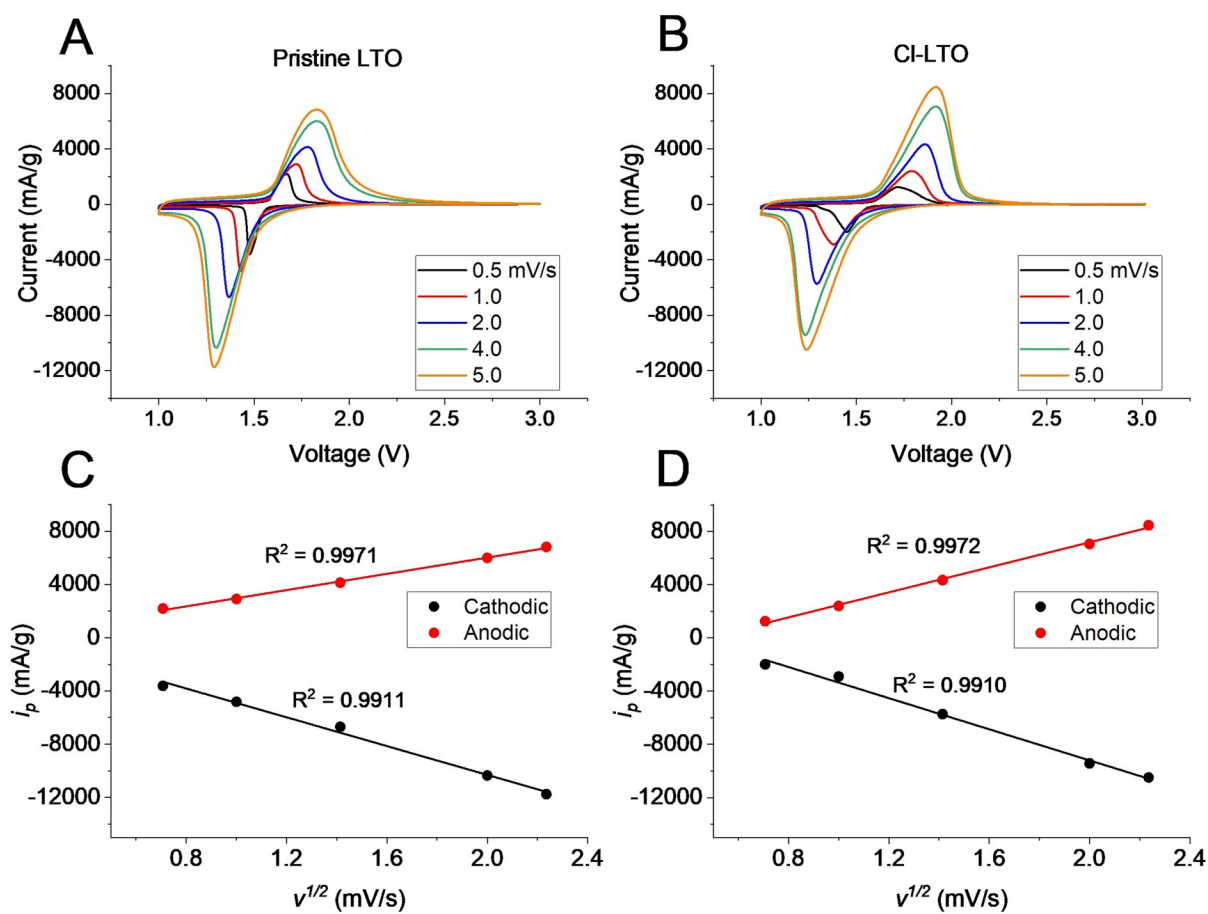


Figure 7. Cyclic voltammograms for (A) pristine LTO and (B) Cl-LTO as a function of scan rate from 0.5–5 mV s^{-1} , as well as the linear fits of the peak current (i_p) as a function of the square root of the scan rate for (C) pristine LTO and (D) Cl-LTO.

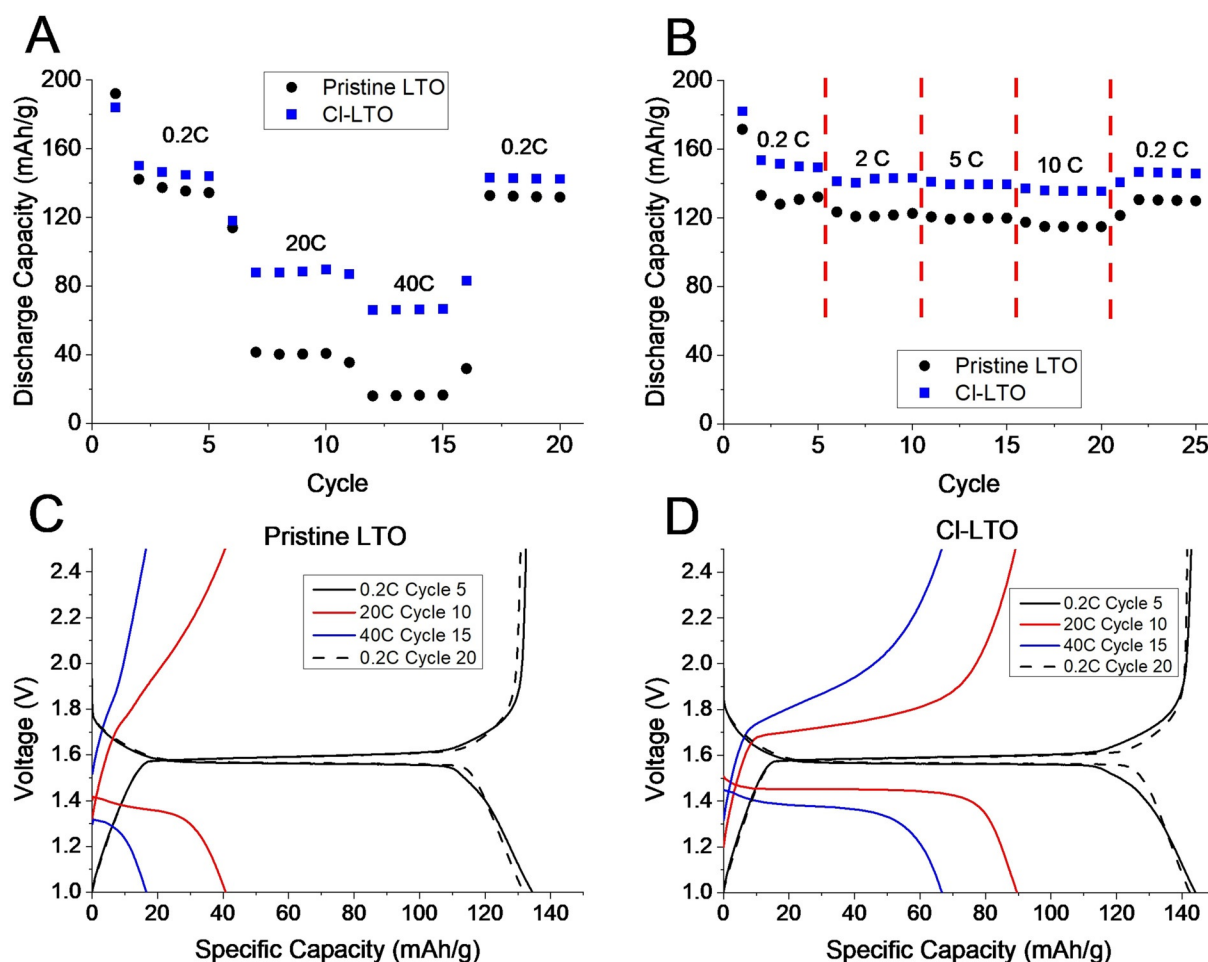


Figure 8. (A–B) Discharge capacity as a function of current density for pristine LTO (black) and Cl-LTO (blue). Voltage profiles for the rate performance of (C) pristine LTO and (D) Cl-LTO, shown in part A.

ples, indicating that they show similar diffusion-controlled behavior during (de)lithiation. In the first cycle, values for the cathodic peak currents for the pristine LTO and Cl-LTO samples are noted as (1.48 V, -3614 mA g^{-1}) and (1.45 V, -1994 mA g^{-1}), whereas anodic peak currents are measured as (1.67 V, 2184 mA g^{-1}) and (1.72 V, 1242 mA g^{-1}), respectively.

The Cl-LTO possessed a higher peak current separation (ΔE_p) of 0.27 V in the first cycle as compared with the pristine LTO (0.19 V). Even so, the ratio of the anodic and cathodic peak currents ($i_{p,a}/i_{p,c}$) in the first cycle for both samples was near 1, indicating reversibility for the Faradaic process. In the fifth cycle, the ratio deviated for both samples. With the pristine LTO, that number decreased to 0.85, whereas for Cl-LTO, it fell to 0.96. This finding can be attributed to a decrease in reversible capacity over time and under faster scan rates for the pristine LTO as well as to a comparatively stable performance of the Cl-LTO, all of which agrees with the following rate performance tests.

The discharge capacities of pristine LTO and Cl-LTO in response to a series of current densities are shown in Figures 8A and B. Cells were cycled 5 times at each rate, returning to the slowest rate at the end of the test. Assuming a 3 electron reduction per formula unit, a slightly lower theoretical capacity is

predicted for the 0.5 mmol Cl-LTO ($174.8 \text{ mA h g}^{-1}$) relative to the unsubstituted LTO ($175.1 \text{ mA h g}^{-1}$). However, the actual observation was of a higher functional capacity for the Cl-LTO throughout the test. Under the low rate (0.2C) test conditions and low cycle numbers (cycles 1 and 2) most representative of theoretical capacity, the Cl-LTO delivered higher functional capacities (182 and 154 mA h g^{-1} , respectively) than the corresponding pristine LTO (172 and 133 mA h g^{-1} , respectively) (Figure 8A). This difference in functional capacity is attributed to improved electronic and ionic access for the Cl-doped material.^[3,49,50] The slight expansion of the lattice due to the Cl-dopant allows for improved Li ion transport,^[14,18,19] and the corresponding increase in Ti^{3+} allows for greater electronic conductivity.^[11,14,18,19] All of these factors contribute to more redox active sites being accessed electrochemically, and can translate to an increase in capacity.

Figure 8A describes the rate capability of the materials, wherein Cl-LTO consistently delivered a higher capacity of 144, 90, 67, and 142 mA h g^{-1} at 0.2, 20, 40, and 0.2C within the 5th, 10th, 15th, and 20th cycles, respectively, as compared with pristine LTO with 134, 41, 17, and 132 mA h g^{-1} , by analogy. The improved performance of the Cl-LTO was most notable at higher rates, similar to previous reports for related Br-doped

LTO systems.^[19] It is plausible and likely that the Cl-LTO may deliver higher capacity due to the replacement of O^{2-} with Cl^- , thereby causing a portion of Ti^{4+} to become Ti^{3+} , due to charge balance considerations. These effects would increase the electrical conductivity of the material, a finding which is in agreement with the DFT calculations and XPS measurements, described previously.^[14–16,19,51]

The voltage profiles for the 5th, 10th, 15th, and 20th cycles for pristine LTO and Cl-LTO are shown in Figures 8C and D, respectively, showing plateaus related to the stable Ti^{4+}/Ti^{3+} reduction. Although both materials maintain reversibility at 0.2C, with a capacity retention of 99% between the 5th and 20th cycles, the pristine LTO loses its voltage plateau upon charge at 20C and upon (dis)charge at 40C. The discharge plateau for Cl-LTO decreased from 1.59 V at 0.2C to 1.45 and 1.39 V at 20C and 40C, respectively. By contrast, the pristine LTO plateau drops from 1.58 V at 0.2C to 1.39 V at 20C before disappearing at 40C. This observation is consistent with the low capacity evinced at higher rates for pristine LTO, which delivered 55% and 75% less capacity at 20C and 40C, respectively, as compared with Cl-LTO.

Additionally, the first discharge at each rate evinces a vastly different capacity than the subsequent four cycles. As an example, the discharge capacity for the Cl-LTO in cycle 11 was 87 mAh g^{-1} , which decreased to 66 mAh g^{-1} in the next cycle. The charge capacity in cycle 10 was 89 mAh g^{-1} at 20 C. Thus, although the rate changed in cycle 11, the structure was more de-lithiated and hence, more capacity was able to be delivered upon the subsequent discharge. However, this does not describe the behavior at the very beginning of testing. The irreversible capacity loss in the first cycle has been previously described as the result of the mechanical failure of a thin surface layer that forms on the outer surface of high-surface area LTO.^[50,52] The occupation of both 16c and 8a sites at the surface can lead to the development of unconventional chemical compositions above $Li_9Ti_5O_{12}$, with a Ti valence state below 3^+ ; this may lead to mechanical failure of the surface layer, an effect that will become more pronounced as size decreases.^[52]

Figure 8B describes the material response to a steady rate change, wherein Cl-LTO also delivered higher capacity as compared with pristine LTO at all rates. In the 5th, 10th, 15th, 20th, and 25th cycles at 0.2C, 2C, 5C, 10C, and 0.2C, the Cl-LTO delivered 149, 143, 139, 135, and 146 mAh g^{-1} , whereas the pristine LTO provided for 132, 123, 120, 115, and 130 mAh g^{-1} , respectively. The highest discharge capacity previously reported for Cl-LTO at a rate of 2C was 120 mAh g^{-1} , which is 16% lower than what is described herein.^[14] This result can be attributed to the complex, hierarchical 3D nanoflower morphology of the Cl-LTO sample analyzed in this work, since such an architecture enhances the amount of available active surface area, thereby allowing for more facile Li ion access to the active material. The capacity retention between the 5th and 25th cycles at 0.2C was 98% for both samples.

The cells used in Figure 7 were subsequently subjected to galvanostatic cycling for 100 cycles at a 2C rate, as displayed in Figure 9. In the 21st cycle, the pristine LTO and Cl-LTO delivered 129 and 141 mAh g^{-1} upon discharge and yielded Cou-

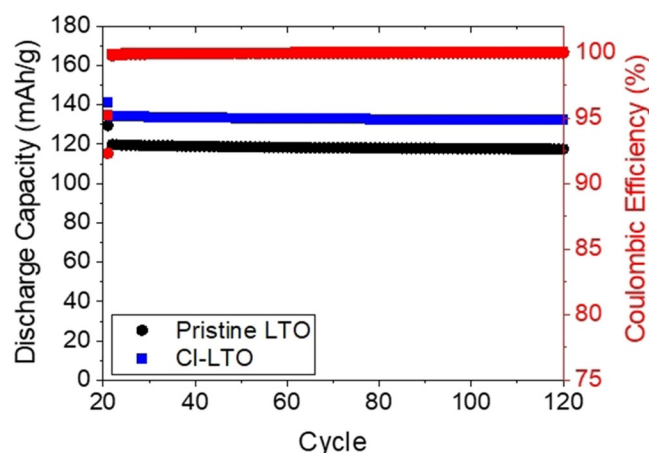


Figure 9. Discharge capacity and Coulombic efficiency for pristine LTO and Cl-LTO over 100 cycles at a 2C rate.

lombic efficiencies of 92% and 95%, respectively. Although the delivered capacity is lower in the subsequent cycle, the capacity between the 21st and 120th cycle is steady, with both samples maintaining capacity retentions of 98%. The pristine LTO and Cl-LTO preserved a 91% and 94% capacity retention between the 21st and 120th cycles, and produced 117 and 132 mAh g^{-1} in the 120th cycle, respectively. Overall, the Cl-LTO possessed a $\approx 12\%$ higher capacity throughout cycling, indicating that the Cl-dopant likely enhances the Li ion transport and/or electrical conductivity of the material, which thereby allows for greater electrochemical access to redox active sites. Notably, the Cl-LTO described in this report generated a $\approx 10\%$ higher capacity in the 50th cycle at a 2C rate as compared with previous literature reports.^[14]

The discharge capacities on 120 cycles for the pristine LTO and Cl-LTO were 117 and 132 mAh g^{-1} , respectively (Figure 9). This is consistent with a 2-electron process for the pristine LTO, because if only 2 Ti^{4+} centers were reduced, a theoretical capacity of 117 mAh g^{-1} would be expected for one $Li_4Ti_5O_{12}$ unit. Based on XPS data, as much as 30% of the total Ti content is described as Ti^{3+} in the Cl-LTO samples. Hence, if one $Li_4Ti_5O_{12}$ formula unit with 30% Ti^{3+} were instead discharged, 175 mAh g^{-1} could still be achieved, since 3.5 Ti^{4+} sites remain in the unit to undergo reduction. Thus, the improvements in the Cl-LTO are attributed to the enhanced electronic and ionic properties of the doped material, thereby allowing for better kinetic access to the redox active sites.

Electrochemical impedance spectroscopy (EIS) was performed before and after electrochemical testing, as shown in Figure 10A–B. Prior to electrochemical tests, there was no semi-circle evident in the high-frequency range for either material. This behavior has been previously noted for vertically-aligned graphene nanosheets, and has been attributed to the ohmic contact of the material to the current collector,^[53] as well as to non-uniform charge storage.^[54,55] Both pristine and Cl-LTO samples are comprised of nanosheets oriented in an urchin-like morphology, which likely gives rise to this previously described behavior.

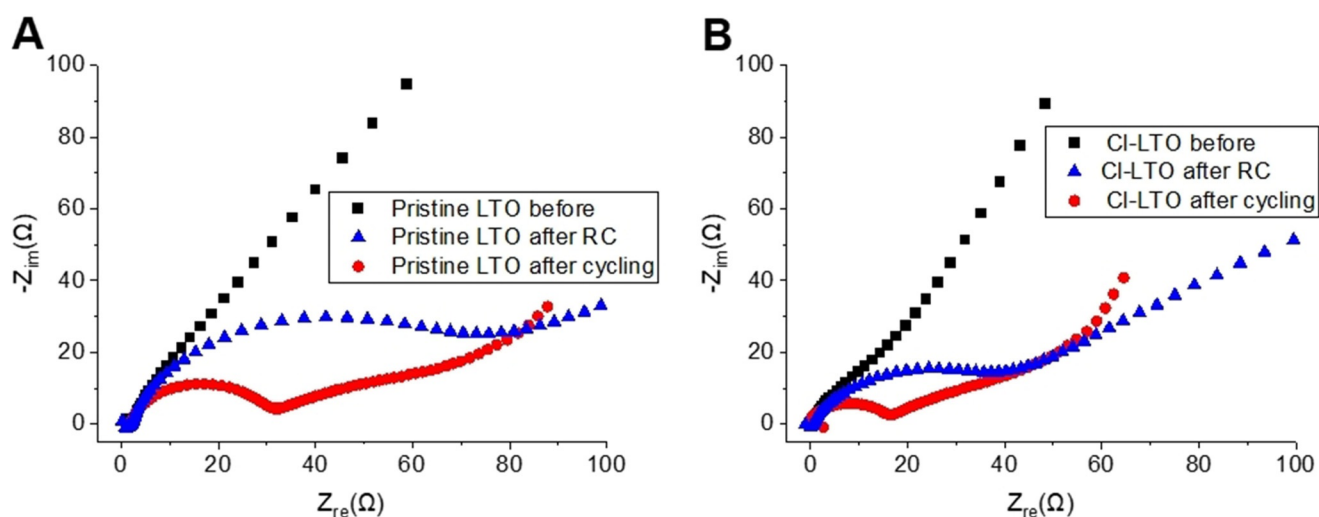


Figure 10. Nyquist plots of electrochemical impedance spectroscopy before testing, after rate capability, and after cycling for (A) pristine LTO and (B) CI-LTO.

The impedance after cycling was fit to the circuit shown in Figure S6 (Supporting Information). The visual fit can be seen in Figure S7. R1 represents the ohmic resistance in the cell, which can be attributed to the solution resistance and electrical resistance of the instrumental set-up and cell components. R2 characterizes the behavior in the mid-to-low frequency range previously ascribed to the Li metal/electrolyte interface in LTO/Li cells.^[56] R3 highlights the charge-transfer resistance of the cathode in the high frequency region. The Warburg element (W_o) describes the diffusion impedance in the low-frequency range, with W_o-T representing the Warburg coefficient which is related to the Li^+ diffusion coefficient through the formula of $W_o-T=L^2/D$ (wherein L is the effective diffusion thickness and D is the effective diffusion coefficient).^[19,57] The CI-LTO sample was characterized by a lower charge transfer resistance and a lower W_o-T value as compared with the pristine LTO (Tables S3–S5), in agreement with the functional capacity results discussed above. Overall, these data support the claim that CI-LTO maintains greater electronic conductivity and enables a more facile Li-ion diffusion, resulting from the slight expansion of the lattice and an increased amount of Ti^{3+} species present in the doped system, thereby ultimately allowing for greater electrochemical access of the material.

Conclusions

In conclusion, 3D nanoflower Cl-doped $\text{Li}_4\text{Ti}_5\text{O}_{12}$ can be successfully synthesized using TBOT as the intended Ti precursor with negligible apparent changes to either chemical composition or morphology. Moreover, our adapted, solution-based synthesis method is much more scalable than that of previous protocols, and will therefore enable the creation of a model system, whereby the fundamental understanding of transport properties can be achieved. We perfected our synthesis conditions, such that 0.40 M LiOH coupled with the use of high purity TBOT generated nanoflower morphologies of LTO at a reasonably large scale per run. Furthermore, the Cl-doping pro-

cess did not damage the intrinsic LTO morphology. Our analysis based on interpreting a compilation of SEM, XRD, XPS, and TEM-EDS results indicated that an optimized dopant amount was 0.5 mmol of Cl. Electrochemical data suggest that the Cl doping of the LTO yielded a $\approx 12\%$ higher capacity throughout cycling, confirming the significance of doping in terms of enhancing Li ion transport and/or electrical conductivity properties of the material, as compared with prior reported literature.

Theoretical calculations were employed to investigate the nature of the Cl dopant within the hexagonal LTO lattice. The dopant Cl caused a distortion of nearby atoms and a slight lattice expansion of 2.75%, due to the large difference between the radius of the Cl^- ion and the O^{2-} ion. As a result, the electronic conductivity and Li diffusion were likely to be improved by partially reducing Ti^{4+} to Ti^{3+} and widening the Li migration channel. Indeed, our XPS data corroborate the assertion that anion-doping, via the directed substitution of O^{2-} with Cl^- , can increase the $\text{Ti}^{3+}/\text{Ti}^{4+}$ ratio.^[14,17,22] Based upon many previous reports, an increase in the $\text{Ti}^{3+}/\text{Ti}^{4+}$ speciation ratio (with its implications for vacancy formation and concomitant need for charge compensation) through rational anionic LTO doping is known to increase capacity by favoring an increase in charge transfer, a corresponding increase in electron conductivity, and a rise in lithium ion diffusion rates.^[6,12,14,16,17,58] Specifically, Cl-doping can activate the adjacent octahedral 16c vacancy for initial Li insertion and thereby facilitate the lithiation activity with an increased cell voltage.

Acknowledgements

All of the work described in these studies was funded as part of the Center for Mesoscale Transport Properties (m2M), an Energy Frontier Research Center supported by the U.S. Department of Energy, Office of Science, Basic Energy Sciences, under award DE-SC0012673. Experimental research characterization was carried out in part at the Center for Functional Nanomate-

rials, Brookhaven National Laboratory (BNL), an Office of Science User Facility, which is supported by the U.S. Department of Energy, Office of Basic Energy Sciences, under Contract No. DE-SC0012704. The DFT calculations were performed using computational resources at the Center for Functional Nanomaterials, which is a U.S. DOE Office of Science Facility, as well as at the Scientific Data and Computing Center, a component of the BNL Computational Science Initiative, at BNL. D.L. acknowledges the support of the National Science Foundation Graduate Research Fellowship under Grant 1839287. Any opinions, findings, and conclusions or recommendations expressed in this material are those of the authors and do not necessarily reflect the views of the National Science Foundation. E.S.T. acknowledges funding from the William and Jane Knapp Chair for Energy and the Environment.

Conflict of interest

The authors declare no conflict of interest.

Keywords: DFT · doping · electrochemical · hydrothermal synthesis · lithium titanium oxide

- [1] F. Wu, X. Li, Z. Wang, H. Guo, *Nanoscale* **2013**, *5*, 6936–6943.
- [2] D. Kong, W. Ren, Y. Luo, Y. Yang, C. Cheng, *J. Mater. Chem. A* **2014**, *2*, 20221–20230.
- [3] J. Ma, C. Wang, S. Wroblewski, *J. Power Sources* **2007**, *164*, 849–856.
- [4] L. Kavan, J. Procházka, T. M. Spítler, M. Kalbáč, M. T. Zúkalová, T. Drezen, M. Grätzel, *J. Electrochem. Soc.* **2003**, *150*, A1000–A1007.
- [5] C. Y. Ouyang, Z. Y. Zhong, M. S. Lei, *Electrochem. Commun.* **2007**, *9*, 1107–1112.
- [6] T.-F. Yi, L.-J. Jiang, J. Shu, C.-B. Yue, R.-S. Zhu, H.-B. Qiao, *J. Phys. Chem. Solids* **2010**, *71*, 1236–1242.
- [7] D. Liu, C. Ouyang, J. Shu, J. Jiang, Z. Wang, L. Chen, *Phys. Status Solidi B* **2006**, *243*, 1835–1841.
- [8] H. Duan, J. Li, H. Du, S. W. Chiang, C. Xu, W. Duan, F. Kang, *J. Phys. Chem. C* **2015**, *119*, 5238–5245.
- [9] Q. Zhang, M. G. Verde, J. K. Seo, X. Li, Y. S. Meng, *J. Power Sources* **2015**, *280*, 355–362.
- [10] Q. Zhang, S. Zhang, F. Ning, X. Lu, Y. Liu, L. Nie, C. Ouyang, L. Zhang, *Energy Technol.* **2017**, *5*, 539–543.
- [11] Z. Yang, J. Wang, Q. Zhang, D. Xiao, B. Xu, A. Zhang, Y. Yu, L. Gu, Y. Hu, H. Li, C. Nan, *Mater. Express* **2015**, *5*, 457–462.
- [12] L. Wang, Y. Zhang, H. Guo, J. Li, E. A. Stach, X. Tong, E. S. Takeuchi, K. J. Takeuchi, P. Liu, A. C. Marschilok, S. S. Wong, *Chem. Mater.* **2018**, *30*, 671–684.
- [13] S. Huang, Z. Wen, Z. Gu, X. Zhu, *Electrochim. Acta* **2005**, *50*, 4057–4062.
- [14] Y. Huang, Y. Qi, D. Jia, X. Wang, Z. Guo, W. I. Cho, *J. Solid State Electrochem.* **2012**, *16*, 2011–2016.
- [15] Y. Charles-Blin, D. Flahaut, J.-B. Ledeuil, K. Guérin, M. Dubois, M. Deschamps, A.-M. Perbost, L. Monconduit, H. Martinez, N. Louvain, *ACS Applied Energy Mater.* **2019**, *2*, 6681–6692.
- [16] Y. Chen, C. Qian, P. Zhang, R. Zhao, J. Lu, M. Chen, *J. Electroanal. Chem.* **2018**, *815*, 123–129.
- [17] G. Du, N. Sharma, V. K. Peterson, J. A. Kimpton, D. Jia, Z. Guo, *Adv. Funct. Mater.* **2011**, *21*, 3990–3997.
- [18] H. Ni, W.-L. Song, L.-Z. Fan, Y.-Z. Wang, *Ionics* **2015**, *21*, 3169–3176.
- [19] Y. Qi, Y. Huang, D. Jia, S.-J. Bao, Z. P. Guo, *Electrochim. Acta* **2009**, *54*, 4772–4776.
- [20] T. Nakajima, A. Ueno, T. Achiha, Y. Ohzawa, M. Endo, *J. Fluorine Chem.* **2009**, *130*, 810–815.
- [21] C. Lin, X. Fan, Y. Xin, F. Cheng, M. O. Lai, H. Zhou, L. Lu, *J. Mater. Chem. A* **2014**, *2*, 9982–9993.
- [22] X. Sun, P. V. Radovanovic, B. Cui, *New J. Chem.* **2015**, *39*, 38–63.
- [23] H. W. Jaffe, *Introduction to Crystal Chemistry*, student edition, Cambridge University Press, Cambridge, United Kingdom, **1988**.
- [24] Y. Wang, Y.-x. Zhang, W.-J. Yang, S. Jiang, X.-w. Hou, R. Guo, W. Liu, P. Huang, J. Lu, H.-t. Gu, J.-y. Xie, *J. Electrochem. Soc.* **2018**, *166*, A5014–A5018.
- [25] Z. Zhao, Y. Xu, M. Ji, H. Zhang, *Electrochim. Acta* **2013**, *109*, 645–650.
- [26] X. Han, Z. Zhao, Y. Xu, D. Liu, H. Zhang, C. Zhao, *RSC Adv.* **2014**, *4*, 41968–41975.
- [27] Y. Ma, B. Ding, G. Ji, J. Y. Lee, *ACS Nano* **2013**, *7*, 10870–10878.
- [28] X. Bai, W. Li, A. Wei, Q. Chang, L. Zhang, Z. Liu, *Solid State Ionics* **2018**, *324*, 13–19.
- [29] J. Wang, Z. Yang, W. Li, X. Zhong, L. Gu, Y. Yu, *J. Power Sources* **2014**, *266*, 323–331.
- [30] Z. Ding, L. Zhao, L. Suo, Y. Jiao, S. Meng, Y. S. Hu, Z. Wang, L. Chen, *Phys. Chem. Chem. Phys.* **2011**, *13*, 15127–15133.
- [31] M. Guo, S. Wang, L.-X. Ding, L. Zheng, H. Wang, *J. Mater. Chem. A* **2015**, *3*, 10753–10759.
- [32] B. Wang, J. Wang, J. Cao, H. Ge, Y. Tang, *J. Power Sources* **2014**, *266*, 150–154.
- [33] H. Utsunomiya, T. Nakajima, Y. Ohzawa, Z. Mazej, B. Žemva, M. Endo, *J. Power Sources* **2010**, *195*, 6805–6810.
- [34] Y. Zhang, Y. Zhang, L. Huang, Z. Zhou, J. Wang, H. Liu, H. Wu, *Electrochim. Acta* **2016**, *195*, 124–133.
- [35] M. Ding, H. Liu, X. Zhao, L. Pang, L. Deng, M. Li, *RSC Adv.* **2017**, *7*, 43894–43904.
- [36] G. Kresse, J. Furthmüller, *Phys. Rev. B* **1996**, *54*, 11169–11186.
- [37] G. Kresse, D. Joubert, *Phys. Rev. B* **1999**, *59*, 1758–1775.
- [38] V. I. Anisimov, J. Zaanen, O. K. Andersen, *Phys. Rev. B* **1991**, *44*, 943–954.
- [39] V. I. Anisimov, F. Aryasetiawan, A. I. Lichtenstein, *J. Phys. Condens. Matter* **1997**, *9*, 767–808.
- [40] S. L. Dudarev, G. A. Botton, S. Y. Savrasov, C. J. Humphreys, A. P. Sutton, *Phys. Rev. B* **1998**, *57*, 1505–1509.
- [41] P. E. Blöchl, *Phys. Rev. B* **1994**, *50*, 17953–17979.
- [42] J. P. Perdew, K. Burke, M. Ernzerhof, *Phys. Rev. Lett.* **1996**, *77*, 3865–3868.
- [43] B. Ziebarth, M. Klinsmann, T. Eckl, C. Elsässer, *Phys. Rev. B* **2014**, *89*, 174301–174308.
- [44] M. G. Verde, L. Baggetto, N. Balke, G. M. Veith, J. K. Seo, Z. Wang, Y. S. Meng, *ACS Nano* **2016**, *10*, 4312–4321.
- [45] M. K. Aydinol, A. F. Kohan, G. Ceder, *Phys. Rev. B* **1997**, *56*, 1354–1365.
- [46] L. Wang, Y. Zhang, C. L. McBean, M. E. Scofield, J. Yin, A. C. Marschilok, K. J. Takeuchi, E. S. Takeuchi, S. S. Wong, *J. Electrochem. Soc.* **2017**, *164*, A524–A534.
- [47] C. H. Lee, S. U. Lee, *J. Phys. Chem. C* **2018**, *122*, 15155–15162.
- [48] W. Zhang, M. Topsakal, C. Cama, C. J. Pelliccione, H. Zhao, S. Ehrlich, L. Wu, Y. Zhu, A. I. Frenkel, K. J. Takeuchi, E. S. Takeuchi, A. C. Marschilok, D. Lu, F. Wang, *J. Am. Chem. Soc.* **2017**, *139*, 16591–16603.
- [49] M. Park, X. Zhang, M. Chung, G. B. Less, A. M. Sastry, *Journal of Power Sources* **2010**, *195*, 7904–7929.
- [50] Y. He, A. Muhetaer, J. Li, F. Wang, C. Liu, Q. Li, D. Xu, *Adv. Energy Mater.* **2017**, *7*, 1700950.
- [51] M. Widmaier, N. Jäckel, M. Zeiger, M. Abuzarli, C. Engel, L. Bommer, V. Presser, *Electrochim. Acta* **2017**, *247*, 1006–1018.
- [52] W. J. H. Borghols, M. Wagemaker, U. Lafont, E. M. Kelder, F. M. Mulder, *J. Am. Chem. Soc.* **2009**, *131*, 17786–17792.
- [53] D. Premathilake, R. A. Outlaw, S. G. Parler, S. M. Butler, J. R. Miller, *Carbon* **2017**, *111*, 231–237.
- [54] Z. Bo, Z. Wen, H. Kim, G. Lu, K. Yu, J. Chen, *Carbon* **2012**, *50*, 4379–4387.
- [55] Q. Cheng, Z. Chen, *Int. J. Electrochem. Sci.* **2013**, *8*, 8282–8290.
- [56] N. Schweikert, H. Hahn, S. Indris, *Phys. Chem. Chem. Phys.* **2011**, *13*, 6234–6240.
- [57] Z. P. Guo, S. Zhong, G. X. Wang, H. K. Liu, S. X. Dou, *J. Alloys Compd.* **2003**, *348*, 231–235.
- [58] S. Nie, C. Li, H. Peng, G. Li, K. Chen, *RSC Adv.* **2015**, *5*, 23278–23282.

Manuscript received: May 20, 2020

Accepted manuscript online: June 25, 2020

Version of record online: July 8, 2020